Available online at www.sciencedirect.com

ScienceDirect

Journal of Magnesium and Alloys 8 (2020) 1047–1060

www.elsevier.com/locate/jma

Full Length Article

High temperature mechanical behaviour of Mg–6Zn–1Y alloy with 1 wt.% calcium addition: Reinforcing effect due to I-($Mg_3Zn_6Y_1$) and $Mg_6Zn_3Ca_2$ phases

J. Medina[a], G. Garces[a], P. Pérez[a,*], A. Stark[b], N. Schell[c], P. Adeva[a]

[a] *Department of Physical Metallurgy, National Center for Metallurgical Research (CENIM-CSIC), Avenida Gregorio del Amo 8, 28040 Madrid, Spain*
[b] *Institute of Materials Research, Helmholtz-Zentrum Geesthacht, Max-Planck-Str. 1, 21502 Geesthacht, Germany*
[c] *Structural Research on New Materials, Helmholtz-Zentrum Geesthacht Outstation at DESY, Notkestraße 85, 22607 Hamburg, Germany*

Received 21 May 2020; received in revised form 29 July 2020; accepted 13 August 2020
Available online 29 September 2020

Abstract

The influence of small calcium additions on the high-temperature mechanical behaviour in an extruded Mg–6Zn–1Y (wt.%) alloy reinforced by the I-phase has been investigated. Calcium promotes the formation of the intermetallic $Mg_6Zn_3Ca_2$ phase instead of I-phase, which results in a noticeable improvement of the yield strength and ultimate tensile strength of the alloy above 100 °C. The strength of the alloys was analysed taking into account the contribution due to the grain size, the crystallographic texture and the volume fraction and nature of second phase particles. In situ synchrotron radiation diffraction experiments have been used to evaluate the load partitioning between the magnesium matrix and the second phase particles (I- and $Mg_6Zn_3Ca_2$ phases) in both alloys. The load transfer from the magnesium matrix towards the $Mg_6Zn_3Ca_2$ phase is markedly more effective than that for the I-phase over the entire temperature range, especially at 200 °C, temperature at which the reinforcement effect of the I-phase is null.

Keywords: Magnesium alloys; I-phase; Synchrotron radiation diffraction; High temperature mechanical properties.

1. Introduction

The development of new magnesium alloys has been increasing in recent years. Several specific characteristics such as low density and high specific strength make it one of the lightest structural metallic materials suitable for use in aerospace and automobile industries [1-3]. An extensive number of high-strength alloy families have been developed through the appropriate choice of alloying elements in proper concentrations. Among them, the Mg–Zn–Y system has a great potential for the design of alloys combining excellent ductility and high strength from room temperature up to 200–250 °C [4-24]. Modifying the ratio between the content of yttrium and zinc, different second phases such as quasicrystalline I-phase ($Mg_3Zn_6Y_1$), W-Phase ($Mg_3Zn_3Y_2$) and Long Period Stacked Ordered (LPSO) phases can be stabilised. The I-phase provides a considerable strengthening to the alloy as result of the strong interface with the magnesium matrix, high hardness and thermal stability until 450 °C [4,25-32]. Furthermore, the alloys containing the I-phase require minor yttrium contents than those alloys containing the LPSO phase, reducing fabrication costs.

The addition of small concentrations of a fourth element to Mg–Zn–Y alloys also contributes to enhance the mechanical properties [19]. The element proposed in the present research is calcium. Its beneficial effect on the mechanical properties, at room and high temperatures, through the formation of hard intermetallic phases has been widely reported [2,22,33-43]. Moreover, calcium not only facilitates recrystallization during extrusion, reducing the typical strong basal texture of wrought

* Corresponding author.
E-mail address: zubiaur@cenim.csic.es (P. Pérez).

https://doi.org/10.1016/j.jma.2020.08.007

magnesium alloys [19,32,44-46], but also increases the ignition temperature of magnesium [47,48].

The present work evaluates the influence of small calcium additions on the increase in the mechanical resistance of Mg–6Zn–1Y (wt.%) alloy at high temperatures. Special emphasis is given to understand the reinforcing capacity provided by second-phase particles and to determine the effectiveness of load transfer from the magnesium matrix towards the second phase particles. For this purpose, synchrotron radiation diffraction experiments during in situ compression tests have been performed. This technique has been extensively used to study the dynamic microstructural processes occurring during deformation of magnesium alloys, providing information on changes in the grain structure, texture evolution, deformation systems, stress–strain behaviour, residual stresses, etc. [49-54]. More specifically, this technique has been used to investigate the reinforcing effect of different second-phase particles in the magnesium alloys, i.e. LPSO-phase [21,24,55-56] as well as the quasicrystalline I-phase in Mg–Zn–Y alloys [57], but the load transfer from the magnesium matrix towards the $Mg_6Zn_3Ca_2$ phase has not been studied yet.

2. Experimental procedure

Ternary Mg–6Zn–1Y (wt.%) alloy, designated as ZW61, was prepared by melting pure magnesium, zinc and yttrium in an electric resistance furnace. This alloy was modified by adding 1% of calcium with a nominal composition of Mg–6Zn–1Y–1Ca (wt.%) and it was designated as ZW61Ca. Both alloys were cast in a cylindrical steel mould of 50 cm in length and 45 mm in diameter and then extruded at 300 °C with an extrusion ratio of 18:1.

Microstructural characterization of extruded ZW61 and ZW61Ca alloys was carried out by Scanning Electron Microscopy (SEM) using a Hitachi S-4800 microscope equipped with an Energy-Dispersive X-ray microanalysis (EDS). Micro-texture analysis was performed by Electron Backscattered Diffraction (EBSD) technique attached to the JEOL JSM 6500F equipment. EBSD data were evaluated using the Channel 5 EBSD software. The Orientation Image Mapping (OIM) was taken in the longitudinal section of the sample, parallel to the extrusion direction (ED) with high angle (> 10°) represented by black lines.

Sample preparation for SEM and EBSD analysis consisted of conventional grinding with silicon carbide followed by mechanical polishing with a solution of colloidal silica in ethanol. Finally, for EBSD analysis, the specimen was chemically etched using a mixture of 3 ml of nitric acid, 7 ml of acetic acid, 10 ml of water and 30 ml of ethanol.

Mechanical properties were evaluated through tensile and in-situ compressive tests. Tensile tests were carried out from room temperature up to 350 °C in a universal tensile machine (Instron model 1362) at an initial strain rate of 10^{-4} s^{-1}. Cylindrical samples were machined from the extruded bar, with a 3 mm radius and gauge length of 10 mm, being the tensile direction parallel to the extrusion direction.

In-situ synchrotron radiation diffraction during compression tests were carried out to evaluate the load partitioning between the I- and $Mg_6Zn_3Ca_2$ phases and the magnesium matrix from room temperature to 200 °C. In-situ experiments were carried out in the P07B -HEMS beamline of PETRA III, at the Deutsches Elektronen-Synchrotron (DESY). It is interesting to point out that extruded magnesium alloys exhibit a different mechanical behaviour under tension and compression due to the activation of tensile twinning in addition to basal slip, although twinning activity tends to disappear as the test temperature increases [58,59]. Consequently, compression tests are perfectly valid to evaluate the reinforcing capacity of the I- and $Mg_6Zn_3Ca_2$ phases during plastic deformation at the temperatures studied in this work. Tests were conducted at a strain rate of 10^{-3} s^{-1}. Experimental details can be extensively found in [57]. The elastic strain for each diffraction peak is calculated by the relative shift in the position of the diffraction peak, as:

$$\varepsilon_{hkl} = \frac{d_{hkl} - d_{0,hkl}}{d_{0,hkl}} \quad (1)$$

where d_{hkl} and $d_{0,hkl}$ are the interplanar distance of the hkl plane in the stressed and stress-free crystal. $d_{0,hkl}$ is selected as the interplanar distance before the compression test. The diffraction angle θ and the lattice planar spacing are linked through the Bragg's law.

$$d_{hkl} = \frac{\lambda}{2\sin\theta_{hkl}} \quad (2)$$

where λ is the wavelength of the radiation (0.0124 nm).

3. Results

3.1. Microstructure

Fig. 1(a–b) shows the back-scattered electron images of extruded ZW61 and ZW61Ca alloys along the ED. The microstructure of the extruded bars is similar in both materials, consisting of a dark magnesium matrix and a bright second-phase aligned along the extrusion direction. The addition of calcium not only changes the nature of the second phase, but also its volume fraction (Table 1). The second phase corresponds mainly to I-phase ($Mg_3Zn_6Y_1$) for the ZW61 alloy and intermetallic $Mg_6Zn_3Ca_2$ phase for the ZW61Ca alloy [32]. The volume fraction of $Mg_6Zn_3Ca_2$ in the ZW61Ca alloy is higher than the volume fraction of I-phase in the ZW61 alloy, but $Mg_6Zn_3Ca_2$ particle size is twice that of the I-phase in ZW61 alloy, 1.2 and 0.6 μm, respectively. It is interesting to note that most of $Mg_6Zn_3Ca_2$ particles are very fine but a small fraction of them is very coarse, with sizes ranging between 5 and 10 μm.

The magnesium matrix in both alloys exhibits a bimodal grain structure consisting of fine equiaxed dynamically recrystallized (DRXed) grains and coarse non-DRXed grains elongated along the extrusion direction (Fig 1c, d). The volume fraction of non-DRXed grains determined from EBSD maps is 7% and 2% for the ZW61 and ZW61Ca alloy, respectively.

Table 1
Microstructural features found in ZW61 and ZW61Ca alloys [32]: volume fraction of second phases ($V_{V\ phase}$), particle size (P_{Size}), volume fraction of non-recrystallized areas ($V_{Vnon\text{-}DRX}$) and grain size of recrystallized grains (GS).

Alloy	$V_{V\ fase}$ (%)	P_{Size} (μm)	$V_{V\ non\text{-}DRX}$ (%)	GS (μm)
ZW61	5.8 ± 0.7	0.6 ± 0.1	7 ± 1	3.6 ± 0.1
ZW61Ca	8.3 ± 1.2	1.2 ± 0.3	2 ± 1	4.4 ± 0.1

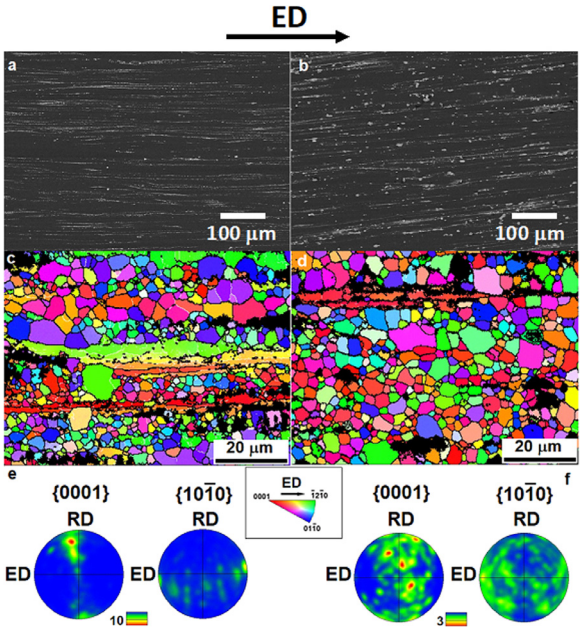

Fig. 1. Backscattered electron images of (a) ZW61 and (b) ZW61Ca alloy. EBSD Orientation Image Mapping (OIM) in the plane of ED (extrusion direction)-RD (radial or transversal direction) and corresponding pole figures of (c, e) ZW61 alloy and (d, f) ZW61Ca alloy.

The average grain size of DRXed grains is 3.6 and 4.4 μm, respectively, for the ZW61 and ZW61Ca alloy. Coarse non-DRXed grains (mainly coloured in green and red in EBSD maps) are highly oriented with their basal planes parallel to the extrusion direction. Fig. 1e and f shows the {0002} and {10$\bar{1}$0} pole figures obtained from the orientation image map in Fig. 1c, d. Both alloys present a typical fibre texture with basal planes parallel to the ED. Texture of the ZW61Ca alloy is less pronounced compared to ZW61 alloy.

3.2. Mechanical properties

The true stress-true strain curves from RT up to 350 °C at a strain rate of 10^{-4} s^{-1} are presented in Fig. 2a and b for ZW61 and ZW61Ca alloys, respectively. Tensile data such as yield stress, ultimate tensile strength and elongation to failure are listed in Table 2.

Tensile behaviour shows two temperature intervals in which both alloys behave in a similar way. In the first interval, from RT to 150 °C, both alloys exhibit certain hardening after yielding that gradually decreases as the test temperature increases. The increase in the test temperature is also accompanied by a gradual decrease in the yield strength and maximum resistance. In the second temperature interval (200–

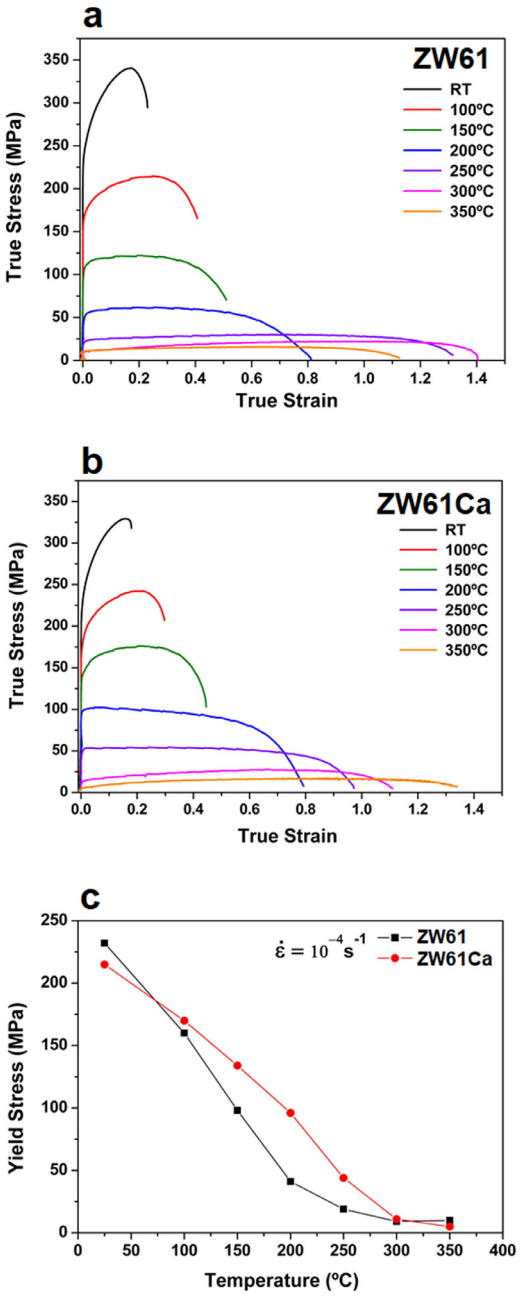

Fig. 2. (a, b) True stress-true strain curves from room temperature up to 350 °C at a strain rate of 10^{-4} s^{-1} for the ZW61 and ZW61Ca alloys, respectively and (c) yield stress dependence with the temperature for both alloys.

Table 2
Yield stress (YS), ultimate tensile strength (UTS) and elongation to failure (EF) values of the extruded ZW61 and ZW61Ca alloys tensile tested from room temperature up to 350 °C.

ALLOY	ZW61			ZW61Ca		
Temperature (°C)	σ0.2 (MPa)	UTS (MPa)	ε (%)	σ0.2 (MPa)	UTS (MPa)	ε (%)
RT	232	340	30	215	329	25
100	160	214	60	170	242	38
150	98	122	83	134	176	60
200	41	62	127	96	102	121
250	19	30	274	44	54	165
300	9	22	309	11	28	206
350	10	16	205	5	17	282

350 °C), the plasticity of both alloys increases considerably, with elongations exceeding 100%, while the yield strength and maximum resistance fall sharply to very low values, even below 20 MPa. The variation of yield strength with the temperature is represented in Fig. 2c. Above 100 °C, the ZW61Ca alloy exhibits higher values of the yield strength compared with the ZW61 alloy, being the maximum difference at 200 °C (2.3 times higher).

3.3. Evolution of the microstructure during plastic deformation

Microstructural evolution during plastic deformation was analysed throughout EBSD maps and their corresponding pole figures obtained at the head of the tensile sample (non-deformed region) and close to the fracture surface (deformed region) of ZW61 and ZW61Ca alloys after tensile testing at 200 and 300 °C (Fig. 3).

At 200 °C, elongated non-DRXed grains of both alloys still coexist with much finer recrystallized regions (Fig. 3a, b, e and f). Non-DRXed grains, coloured in green and red, are oriented with the basal planes parallel to the extrusion direction, which contribute to increase the basal texture, as can be observed in the corresponding pole figures, while fine DRXed grains are randomly oriented.

At 300 °C, the microstructure of both extruded alloys undergoes relevant changes. On one hand, grain size increases with respect to the as-extruded condition reaching values of up to 30 and 20 μm for ZW61 and ZW61Ca alloys, respectively. On the other hand, non-DRXed regions initially existing disappear completely in the course of plastic deformation, leading to an equiaxed grain structure (Fig. 3d and h). Thus, pole figures indicate that the equiaxial grains are randomly oriented softening the overall texture especially in ZW61Ca alloy. In ZW61 alloy, it can be noticed that the intensity of the texture is higher at 300 °C than that at 200 °C.

Fig. 4 shows backscattered SEM images of longitudinal sections for the ZW61 alloy and the ZW61Ca alloy deformed at RT, 200 and 300 °C. Although the nature, morphology and size of the second phases is different, both alloys present similar microstructural features prior to and after deformation. In non-deformed regions, i.e. in the as-extruded condition, linear arrangements of I-phase/$Mg_6Zn_3Ca_2$ particles appear aligned along the extrusion direction (Fig. 4a and b). This microstructure evolves during deformation disregarding test temperature. Thus, samples deformed at room temperature exhibits short cracks confined within the linear arrangements of I-phase/$Mg_6Zn_3Ca_2$ particles running perpendicularly to the loading direction without penetrating into the adjacent magnesium matrix (Fig. 4c and d). It is interesting to note that cracks are preferentially associated with coarse second phase particles, so cracking is more pronounced for ZW61Ca alloy than for ZW61 alloy. As the temperature increases, the perfect linearity of second phase arrangements is progressively broken during deformation. Particles are laterally shifted from their original position in the linear arrangements, being such displacement more pronounced as the test temperature increases. Thus, particles are hardly displaced after deformation at 200 °C (see Fig. 4e and f), but they are more uniformly distributed after deformation at 300 °C, especially in the regions close to the fracture. In addition, cracks are mainly linear at low temperatures and they are aligned along the extrusion direction (see Fig. 4e and f). It seems that the origin of long cracks is the perpendicular flaws/cracks nucleated in the coarse I-phase or $Mg_6Zn_3Ca_2$ particles. Further loading leads to the separation between both parts of the cracked particles along the applied stress direction, resulting in the development of long linear cracks. With increasing temperature, the volume fraction of cracks increases as well as their size (see Fig. 4g and h). Now, cracks/cavities are not linear, and they can progress not only along the loading direction, but also perpendicularly to it.

3.4. Evolution of the internal stress in the second phases

Fig. 5a–d shows diffraction patterns as a function of 2θ, obtained integrating Debye-Scherrer rings along the axial and radial directions, acquired before (Fig. 5a and c) and after (Fig. 5b and d) the in-situ compression test for the extruded ZW61 and ZW61Ca alloys. On Fig. 5a and c, in the axial direction, owing to the intense fibre texture of the alloy, the diffraction peak corresponding to the $\{10\bar{1}0\}$ planes exhibits the highest intensity, being more intense in the case of the ZW61 alloy. In contrast, the intensity of the diffraction peak corresponding to (0002) plane in the axial direction is very low. This behaviour is inverted in the diffraction pattern

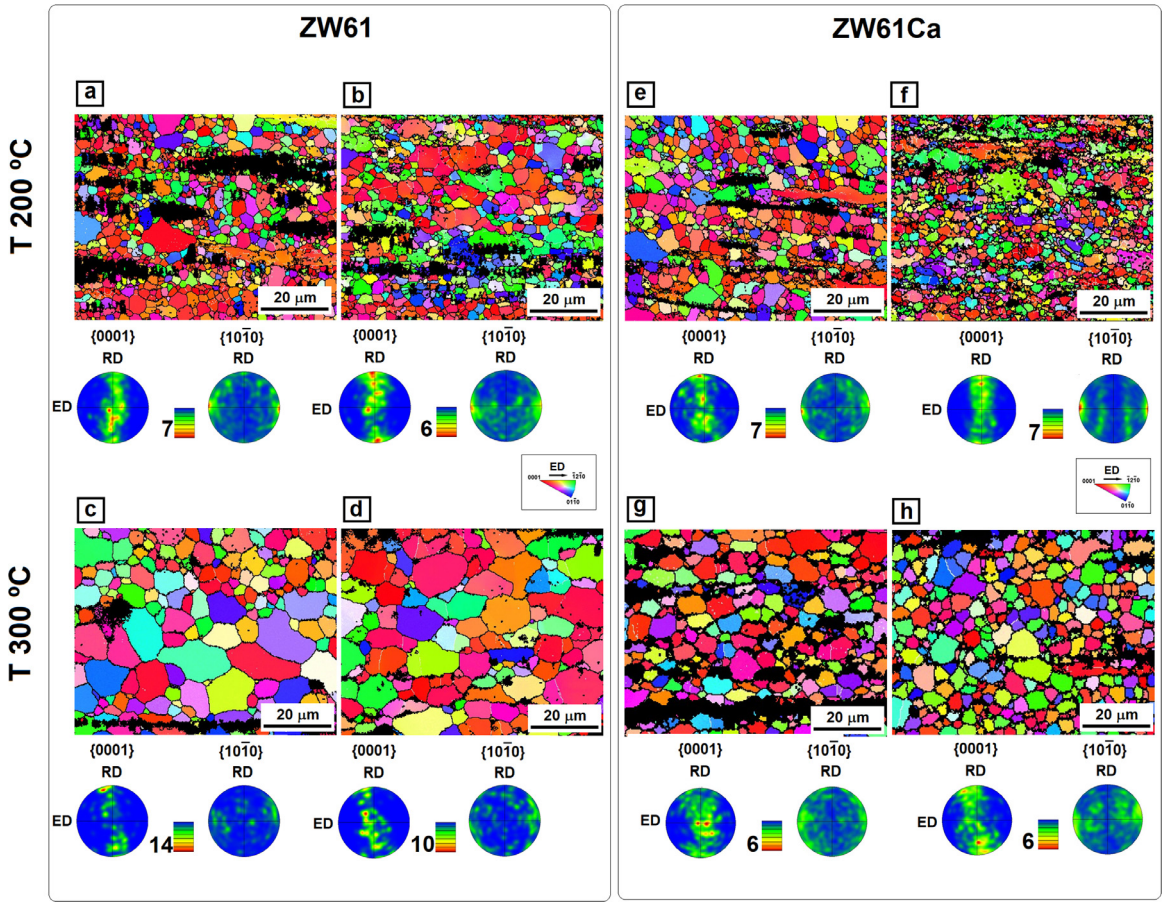

Fig. 3. EBSD Orientation Image Mapping (OIM) in the plane of ED-RD and pole figures of the extruded ZW61 and ZW61Ca alloys tested at 200 and 300 °C in the (a, c, e, g) non-deformed and (b, d, f, h) deformed regions.

obtained in the radial direction. The diffraction peaks corresponding to the second phases are also detected (see insets in the plots). In the ZW61 alloy, the most intense diffraction peak of the I-phase appears at $2\theta = 3.04°$ corresponding to the {221,001} diffraction peak (in Elser indexes [60,61] used for quasicrystal). For the ZW61Ca alloy, the main diffraction peak of the $Mg_6Zn_3Ca_2$ phase corresponds to {222} plane at $2\theta = 3.3°$. Despite its low intensity, it can be fitted accurately. After compression tests, diffraction peaks are shifted to higher 2θ values (lower d values) and the intensity of the diffraction peaks changes significantly (Fig. 5b and d). The intensity of the (0002) diffraction peak strongly increases at expenses of the {10$\bar{1}$0} diffraction peak due to activation of tensile twinning [57,59,62,63]. The evolution of the elastic strains was calculated using Eq. (1). d_0 was assumed as the d value at zero external stress, i.e. before the compression test.

The evolution of the elastic strains, between room temperature and 200 °C, has been evaluated for {10$\bar{1}$0}, {0002}, {10$\bar{1}$1} and {11$\bar{2}$0} diffraction peaks of magnesium. {221,001} diffraction peak of the I-phase and the {222} diffraction peak of $Mg_6Zn_3Ca_2$ have been considered for the calculation of internal strains in each of these phases. Fig. 6 (a–f) shows the evolution of the elastic strains as a function of the applied stress in the axial direction for both phases: the magnesium matrix and the I-phase in ZW61 alloy and the magnesium matrix and the $Mg_6Zn_3Ca_2$ phase in ZW61Ca alloy. This temperature range has been chosen because in it differences in yield stress are maximum between ZW61 and ZW61Ca alloys. At 300 °C, however, variation in the yield stress among the alloys are almost negligible, as can be seen in Fig. 2c. The engineering compression curves for both alloys at RT, 100 and 200 °C are also shown in Fig. 6. These compressive curves allow an easy comparison of macroscopic strains and specific-planar strains in each family of planes. At room temperature, the macroscopic yield stress, corresponding to the 0.2% of plastic deformation, is around 200 MPa in both alloys. However, the yield stress is always higher for the ZW61Ca alloy as the temperature increases. Moreover, the stress gap becomes progressively higher as the test temperature increases, which is the same behaviour found during tensile testing (see Fig. 2). Finally, Fig. 6(a–f) shows the integrated intensity along the axial direction for {10$\bar{1}$0} and (0002) diffracted peaks as a function of the applied stress. As it was commented before, the intensity evolution of both orientations is connected due to the activation of the twinning [57,59,62,63]. In addition, it is necessary to know how precisely the elastic strain in the magnesium matrix evolves in these alloys with a bimodal grain structure as the temperature increases as a way for identifying the deformation mechanism. Below the macroscopic yield stress, both alloys behave purely elastically, following

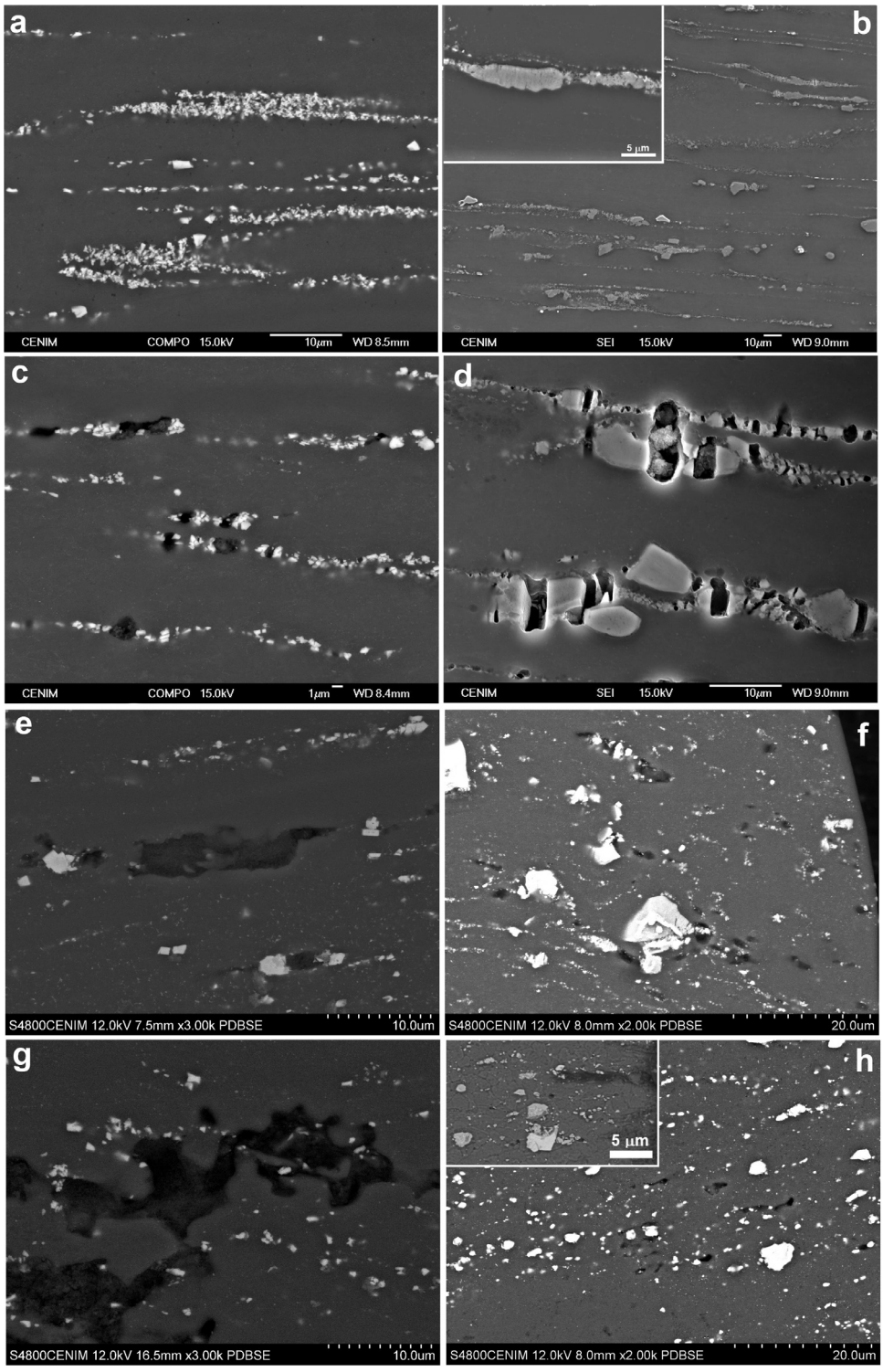

Fig. 4. Longitudinal views of (a, b) non-deformed and (c, d, e, f, g, h) deformed regions of samples tested at room temperature (c, d), 200 °C (e, f) and 300 °C (g, h) for the ZW61 alloy (a, c, e, g) and ZW61Ca alloy (b, d, f, h).

the same slope. However, the applied stress dependence of elastic strains for some diffraction peaks loses their linearity before reaching the macroscopic yield. For both alloys, first deviation from linearity is found for grains oriented with the $\{10\bar{1}1\}$ plane perpendicular to the compression axis (see blue arrows in Fig. 6) regardless of the testing temperature. These grains are favourably oriented for the activation of basal slip with a Schmid factor of 0.43. As expected, the microyielding stress for these grains decreases as temperature increases. This deformation mechanism is independent on the stress sign and, consequently, it should be also activated under tension along the extrusion direction. Second deviation from linearity

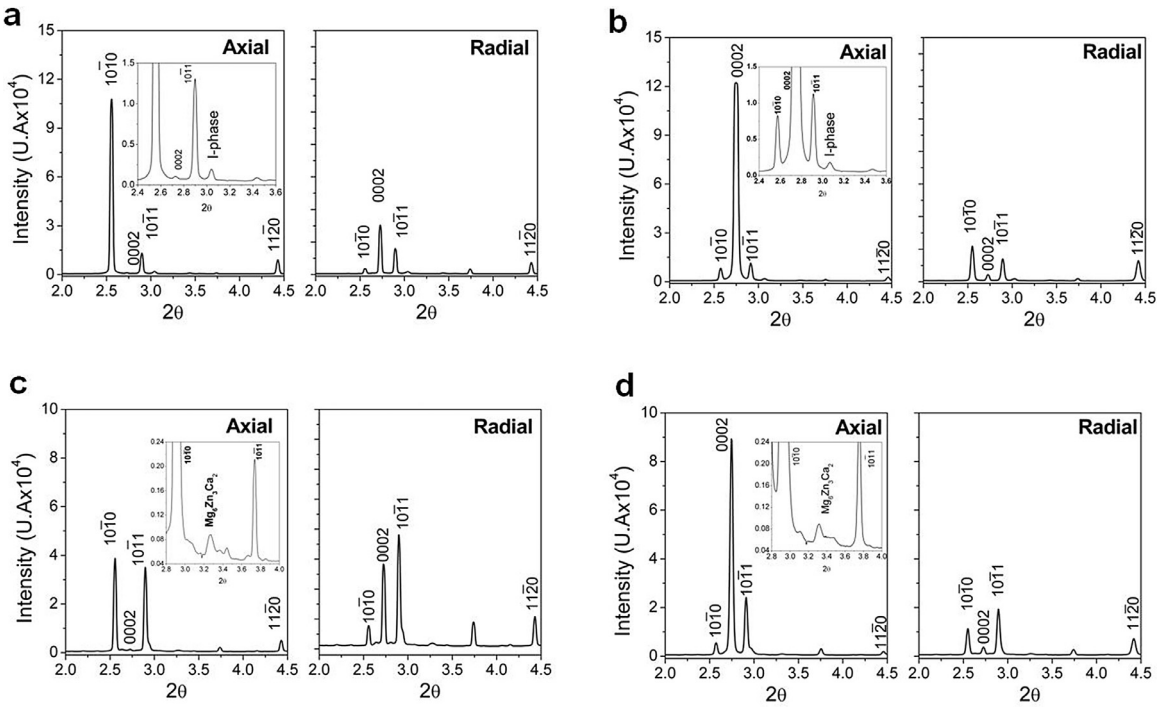

Fig. 5. Diffraction patterns as a function of 2θ along the axial and radial directions obtained by integration of Debye–Scherrer rings, (a, c) before and (b, d) after the in-situ compression test for the (a, b) ZW61 and (c, d) ZW61Ca alloys, respectively.

is observed for grains oriented with their (0002) plane perpendicular to the compression axis (see red arrows in Fig. 6). In the region between micro-yielding and macroscopic yield stress, the elastic strain decreases a little (in absolute values). Above macroscopic yield stress, the elastic strain of the (0002) increases (in absolute value) again with a higher rate compared to the rate observed in the elastic regime, which is accompanied with the continuous increase in the integrated intensity (Fig. 6a–b). This simultaneous change in the integrated intensity of the $\{10\bar{1}0\}$ and (0002) diffraction peaks is related to the nucleation, propagation and further growth of twins [57,59,62,63]. Finally, magnesium grains oriented with $\{10\bar{1}0\}$ and $\{11\bar{2}0\}$ planes perpendicular to the compression axis are not favourably oriented for basal slip. The Schmid factor for the slip of ⟨a⟩ dislocations in the basal plane is zero for both grain orientations. Therefore, the evolution of the elastic strains as a function of the applied stress should remain linear-elastic during the compression test when no other slip systems are activated.

The evolution of elastic strains of the second phases (I-phase in the ZW61 alloy and $Mg_6Zn_3Ca_2$ phase in the ZW61Ca alloy) are also presented in Fig. 6. At room temperature, the I-phase and $Mg_6Zn_3Ca_2$ phases show a linear behaviour up to the macroscopic yield stress with a slope higher than that for the magnesium phase. Assuming an "isostress" approach, the Young modulus can be estimated as 66 GPa and 50.5 GPa, for the I-phase and $Mg_6Zn_3Ca_2$ phase, respectively. The Young modulus of both intermetallic phases is higher than that of magnesium (45 GPa [64]). After the yielding of the magnesium matrix, the internal strain of intermetallic phases significantly decreases (in absolute values), particularly just after yielding. The elastic strain measured in the $Mg_6Zn_3Ca_2$ phase is higher than in the I-phase for identical applied stresses. Thus, at 8% of plastic strain, the internal strains are −0.009 and −0.014 for the I-phase and $Mg_6Zn_3Ca_2$ phases, respectively. At 100 °C, the behaviour is similar to room temperature. However, while the internal strain in the $Mg_6Zn_3Ca_2$ phase is equal to the values obtained at room temperature, the internal strain of the I-phase decreases (−0.005 at 10% of strain) even below the internal strain value of grains oriented with the basal plane perpendicular to the loading axis (twins). At 200 °C, the elastic strains in the $Mg_6Zn_3Ca_2$ phase decreases with respect to room temperature and 100 °C (−0.0075 at 10% of strain). In the ZW61 alloy, the internal strains of the I-phase are lower than the values calculated for all diffraction peaks of the magnesium phase.

From the elastic strains (Fig. 6), the internal stress along the axial direction of the intermetallic phases can be evaluated using the generalized Hookeś equation:

$$\sigma_{tot,ax} = \frac{E_{hkl}}{(1-2\nu_{hkl})(1+\nu_{hkl})}\left[(1-\nu_{hkl})\varepsilon_{tot,ax} + 2\nu_{hkl}\varepsilon_{tot,rad}\right] \quad (3)$$

where E and ν are the Young Modulus and Poisson ratio of the hkl plane. The load partitioning between each family of magnesium grains depends strongly on their individual crystallographic orientation. However, the average stress in the magnesium phase can be calculated using the stress balance between the magnesium matrix and the second phases by assuming that the stress in the I-phase and $Mg_6Zn_3Ca_2$ phase

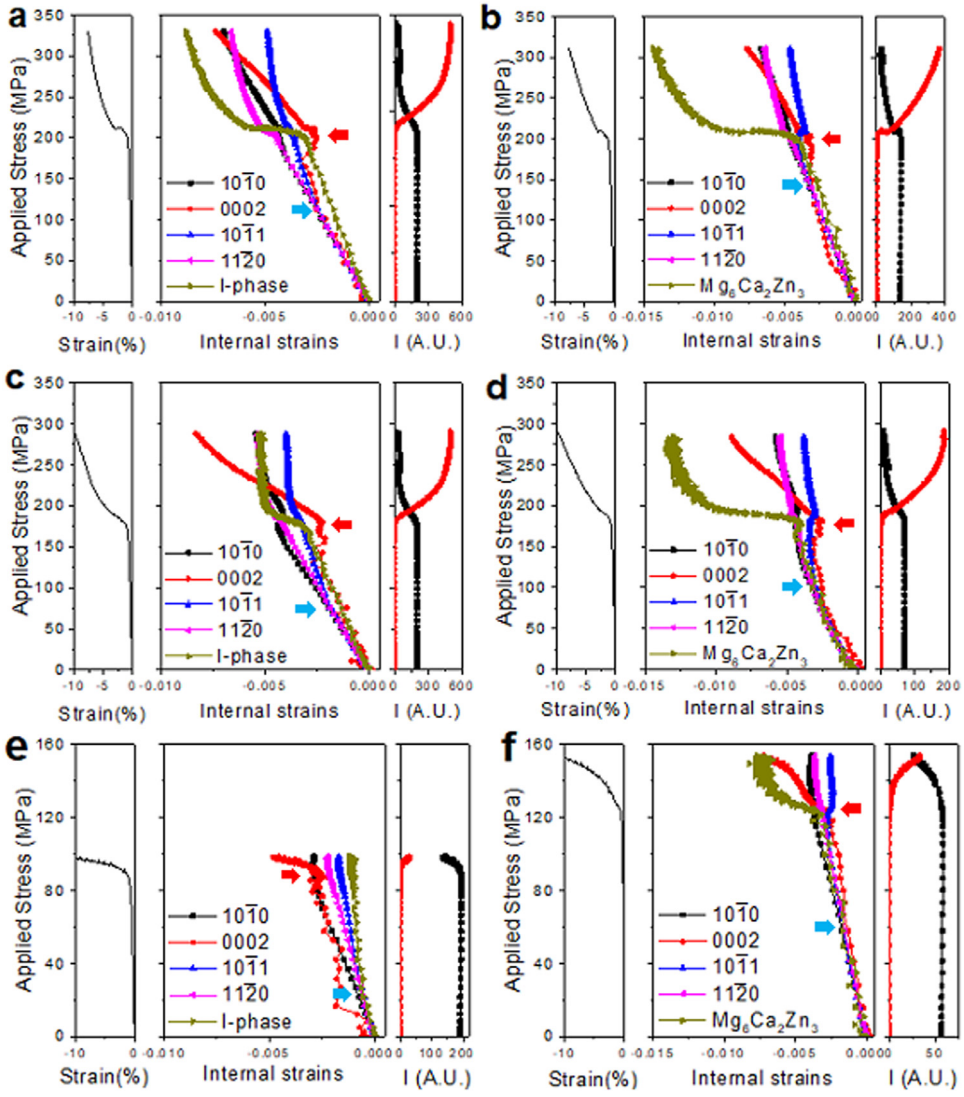

Fig. 6. Compressive macroscopic stress-strain curve, evolution of the elastic strains as a function of the applied stress in the axial direction and integrated intensity in the axial direction of the diffracted peaks obtained during the in-situ compression tests from (a, b) room temperature, (c, d) 100 °C and (e, f) 200 °C for (a, c, e) ZW61 alloy and (b, d, f) ZW61Ca alloy.

is homogeneous, since they behave pure elastically.

$$\sigma_{app} = f_{int}\sigma_{int} + (1 - f_{int})\sigma_{Mg} \quad (4)$$

This method has been successfully applied for evaluating the stress evolution during thermal cycles at high temperature in aluminium matrix composites or the residual stresses in magnesium matrix composites [65-68].

The Young modulus and Poisson ratio of the I-phase and $Mg_6Zn_3Ca_2$ phases and its evolution with the temperature is not reported in the literature. Takeuchi and Edagawa [69] reported an estimation of the Young modulus and Poisson ratio of the I-phase ($E = 112$ GPa and $\nu = 0.208$) at room temperature. However, values obtained from the slope of the elastic strain versus applies stress in the elastic regime are much lower. On the other hand, E and ν values obtained for the $Mg_6Zn_3Ca_2$ phase are in the range of intermetallic Mg-RE compounds [70,71]. In this work, the experimental Young modulus obtained from Fig. 6 and a Poisson ratio of 0.2 has been used. Fig. 7(a, b) shows the evolution of the internal stresses in both phases for both alloys at room temperature, 100 °C and 200 °C. The compression curves are also plotted for an easy comparison. Moreover, the function $\sigma_{app} = \sigma_{int}$ (dash black line in the plot) has been equally included. This line establishes the boundary where the phase bear higher (right side) or lower (left side) loads than the applied stress.

Load transfer has been evaluated during compression tests. Although magnesium alloys exhibit tension/compression asymmetry which is noticed by the different shapes of tension and compression curves. In compression curves, the typical flat region, immediately after the yield stress, is followed by a linear hardening stage during subsequent deformation in the plastic regime. Both features denote the activation of twinning at room temperature and 100 °C. While a large difference between the yield stress in tension and compression is found at room temperature, indicative of the significant contribution of twinning for softening the material, such difference has

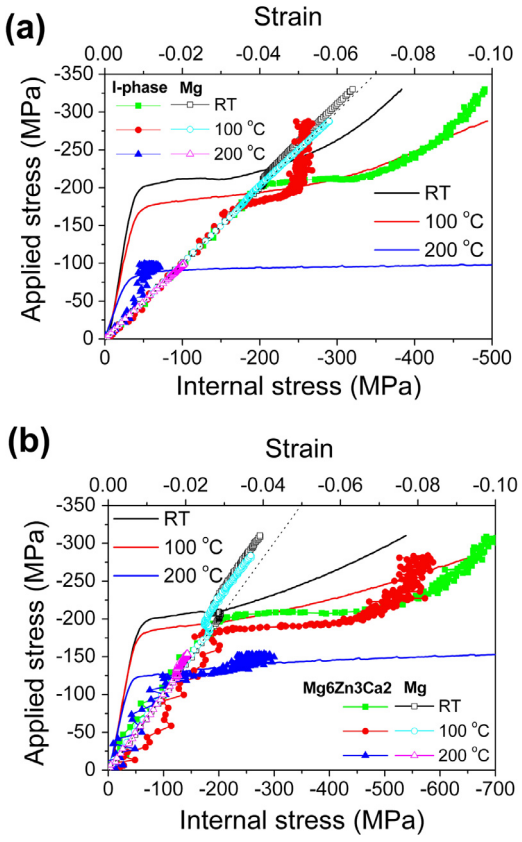

Fig. 7. Evolution of the internal stresses in (a) I-phase for ZW61 alloy and (b) $Mg_6Zn_3Ca_2$ phase for ZW61Ca alloy, at room temperature, 100 °C and 200 °C.

almost disappeared at 100 °C, denoting low contribution of twinning mechanism. At 200 °C, deformation is exclusively controlled by dislocation motion. Consequently, it can be assumed negligible contribution of twinning during deformation at 100 and 200 °C. In compression curves, the stress in the magnesium and I-phase at room temperature follows a linear behaviour with a slope near 1 below the yield stress (Fig. 7a). Above the yield stress, the evolution in the stress of the magnesium phase deviates from the linearity towards lower values (in absolute values). Contrarily, the stress born by the I-phase increases rapidly up to almost 340 MPa for a strain of 3% (the stress in the magnesium phase is about 205 MPa and the applied stress is 211 MPa) and close to 490 MPa for a strain of about 8% (the stress for the magnesium phase is about 320 MPa and the applied stress is 331 MPa). At 100 °C, the behaviour is similar to room temperature. The stress assumed by the I-phase rapidly increases up to 250 MPa once the yield stress is surpassed. This is the maximum stress that can bear the I-phase, because this value remains constant beyond the 4% of total strain. Thus, for strains exceeding the 4%, the increase of stress is assumed by the matrix. Thus, at 4% of strain the stress in the I-phase is 250 MPa, about 190 MPa in the magnesium phase and the applied load is 194 MPa while at 10% the stresses are 263 MPa for the I-phase, 290 MPa for the magnesium matrix and 287 MPa the applied load. At 200 °C, the stress in the I-phase is always lower than the applied stress. Therefore, the I-phase is not effective reinforcing magnesium at 200 °C.

In the ZW61Ca alloy, similar to the ZW61 alloy, the stress in the $Mg_6Zn_3Ca_2$ and the magnesium phases for all temperatures follows a linear behaviour with a slope near 1 below yield stress. Above yield stress, the evolution in the stress of the magnesium phase deviates from the linear behaviour to lower values (in absolute values). Moreover, the magnitude of such deviation is higher than that found for the I-phase. On the contrary, the stress bear by the $Mg_6Zn_3Ca_2$ is at least two times higher than that of magnesium for a given strain. At room temperature, the $Mg_6Zn_3Ca_2$ particles withstand about 510 MPa when the sample is compressed 3%, while the stress in the magnesium matrix is 188 MPa just and the applied load 215 MPa. At strain of 8%, $Mg_6Zn_3Ca_2$ phase withstands almost 700 MPa, the magnesium matrix 273 MPa and the applied stress is 310 MPa. At 100 °C, at strain of 3%, the stress assumed by the $Mg_6Zn_3Ca_2$ phase is about 420 MPa, the magnesium withstands 174 MPa and the applied load is 195 MPa. The load assumed by the $Mg_6Zn_3Ca_2$ phase increases more slowly with progressing plastic deformation up to 570 MPa at strain of 10%, while the stress in the magnesium matrix is 257 MPa and the applied load is 283 MPa. At 200 °C, $Mg_6Zn_3Ca_2$ particles continue reinforcing the material during the entire plastic regime. The stress bear increases gradually with plastic deformation up to about 300 MPa at strain of 10%. At this strain the stress assumed by the magnesium matrix is lower than the applied stress, 142 and 154 MPa, respectively. These data reveal that the $Mg_6Zn_3Ca_2$ phase is an effective reinforcement of magnesium over the entire temperature range (RT-200 °C).

To elucidate if hardening is related to the nature or volume fraction of second phases, or even a combination of them, the load assumed (from curves plotted in Fig. 7.) by 1% in volume fraction of the I- and $Mg_6Zn_3Ca_2$ phases has been calculated. At room temperature, the values are very similar; load assumed by the 1% in volume fraction of second phase is 58.62 MPa and 61.44 MPa, respectively, for the ZW61 alloy and for the ZW61Ca alloy. Second-phase volume fraction prevails over their nature. At 100 °C, however, the load assumed by the second phase decreases, but it becomes higher for the alloy reinforced by the $Mg_6Zn_3Ca_2$ phase. Thus, the load assumed by 1% in volume fraction of I-phase and $Mg_6Zn_3Ca_2$ is 43.10 and 50.60 MPa, respectively. Despite the hardening associated with the volume fraction is still important, the nature of the phase tends to be more important. At 200 °C, the load assumed by the I-phase is smaller than the applied load, thus the reinforcement effect of the I-phase is null. In the case of $Mg_6Zn_3Ca_2$ the load assumed by 1% of this phase is 36 MPa. Therefore, the nature of the second phase prevails over its volume fraction.

4. Discussion

The tensile behaviour at room temperature of extruded ZW61 and ZW61Ca alloys were studied in a previous work [19]. The strength of the alloys was analysed considering

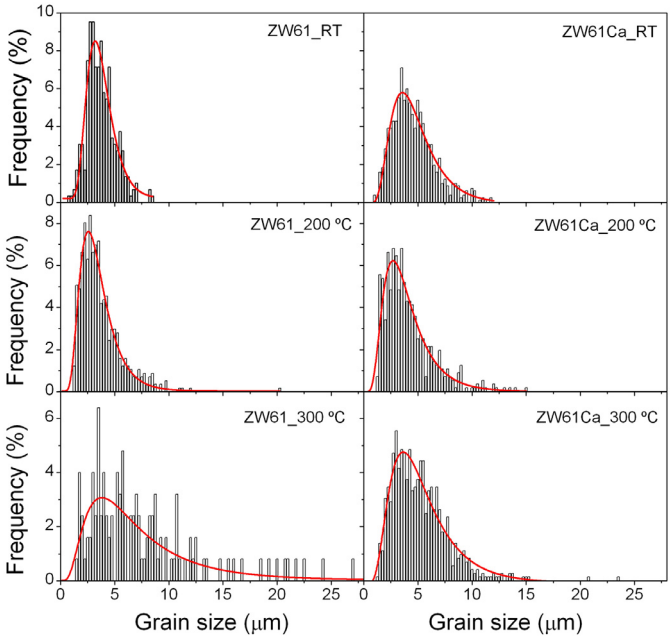

Fig. 8. Histograms of the grain size distribution in the non-deformed area for ZW61 and ZW61Ca alloys at room temperature (RT), 200 and 300 °C.

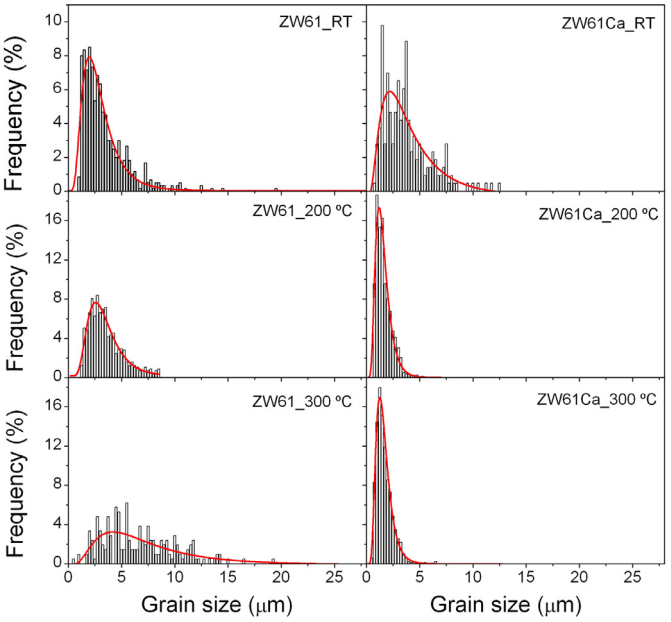

Fig. 9. Histograms of the grain size distribution in the deformed area for ZW61 and ZW61Ca alloys at room temperature (RT), 200 and 300 °C.

three main contributions: grain size, coarse second phases located at grain boundaries and fine precipitates within magnesium grains. The grain size contribution calculated by the Hall–Petch equation and the strengthening due to fine precipitates within magnesium grains, calculated according to Orowan equation, are similar in both alloys. The hardening induced by coarse second phases was greatest in ZW61Ca alloy, since Vickers hardness of $Mg_6Zn_3Ca_2$ phase was superior to the I-phase [19,32]. Nevertheless, the yield stress at room temperature of ZW61 alloy was somewhat greater than that of the ZW61Ca alloy, mainly due to a greater presence of non-DRXed areas in the ternary alloy. These grains, highly oriented with their basal planes parallel to the extrusion direction, prevent basal slip at room temperature, contributing to increase the yield stress of the alloy. However, the present study evidences that calcium addition improves noticeably the mechanical properties of the ternary alloy in the temperature range 100–300 °C (Fig. 2c). The analysis of hardening contributions at high temperature cannot be carried out following the same arguments as at room temperature, since the increase in the temperature introduce new considerations in the three contributions described above.

Grain size refinement could facilitate at high temperature the activation of grain boundary sliding (GBS) mechanism in magnesium alloy, which would result in a noticeable drop in the flow stress. Furthermore, the grain can grow during tensile testing by effect of temperature and /or strain. Thermal stability of the grain was evaluated after tensile testing on the head of the samples (Fig. 8) as well as on the gauge length (Fig. 9). Calculated values of the grain size are listed in Table 3. The grain size in the head, i.e. non-deformed areas, obeys a log-normal distribution in all cases. Compared with room temperature results, the grain size at 200 °C does not grow during tensile testing: 3.6 μm and 4 μm for ZW61 and ZW61Ca alloys, respectively, similar to the grain size in the as-extruded condition. However, at 300 °C, the grain size of ZW61 alloy experiences a moderate growth, with an average size of 7.6 μm, while grain growth is lower for the ZW61Ca alloy, with an average size of 5.1 μm.

According to the creep equation used to study the mechanisms involved at high temperatures, there is a direct relationship between the grain size and the flow stress [72]:

$$\dot{\varepsilon} = A\left(\frac{b}{d}\right)^{p}\left(\frac{GbD}{KT}\right)\left(\frac{\sigma}{G}\right)^{n} exp\left(\frac{-Q}{RT}\right) \quad (5)$$

where A is a material parameter, b is the Burgers vector, G is the shear modulus, D is the diffusion coefficient, σ is the applied stress, d is the grain size, K is the Boltzmann's constant, T is the temperature, Q is the creep-activation energy, R is the universal gas constant, p is a dimensionless constant and n is the stress exponent. Thus, for a given strain rate, a smaller grain size implies lower stresses. At 200 °C, the grain size of ZW61Ca alloy remains smaller than the ternary ZW61 alloy, which would imply a decrease in the mechanical strength due to calcium addition. However, experimental data evidences the opposite behaviour; the ZW61Ca alloy exhibits higher yield stresses than ZW61 alloy (Fig. 2c). Therefore, the better mechanical properties of the calcium containing alloy at 200 °C could not be attributed specifically to the hardening contribution provided by the grain size.

The contribution to the reinforcement of the alloy caused by the non-DRXed areas (*texture contribution*) is no longer as effective at high temperatures; not only because its volume fraction is reduced due to dynamic recrystallization during deformation, but also because, as mentioned above, at

Table 3
Average grain size in the head (non-deformed areas) and the fracture (deformed areas) of the tensile samples for ZW61 and ZW61Ca alloys.

T (°C)	ZW61		ZW61Ca	
	GS $_{Head}$ (μm)	GS $_{Fracture}$ (μm)	GS $_{Head}$ (μm)	GS $_{Fracture}$ (μm)
RT	3.6 ± 0.1	3.3 ± 0.1	4.4 ± 0.1	3.6 ± 0.1
200	3.6 ± 0.1	2.5 ± 0.1	4.0 ± 0.1	1.5 ± 0.1
300	7.6 ± 0.1	6.4 ± 0.1	5.1 ± 0.1	1.5 ± 0.1

high temperatures other slip systems such as non-basal ⟨a⟩ and pyramidal ⟨$c+a$⟩ slip systems could be more easily activated. The addition of calcium decreases the critical resolved shear stress (CRSS) of the prismatic slip and the ratio CRSS($\tau_{Prismatic}/\tau_{Basal}$) [73-75]. Moreover, as the temperature increases, CRRSs of non-basal slip systems decreases significantly. Therefore, grains with basal planes parallel to the extrusion direction no longer contribute to reinforce the alloy.

At this point, the improvement of the mechanical properties at high temperature provided by calcium additions cannot be explained neither by the grain size nor texture contributions. Therefore, the higher reinforcing capacity of the $Mg_6Zn_3Ca_2$ phase with respect to the I-phase, especially at 200 °C, has to account for the yield stress difference between both alloys. The Young's modulus of I-phase and $Mg_6Zn_3Ca_2$ are higher than that of magnesium, so second-phase particles can bear an additional load transferred from the magnesium matrix during plastic deformation. Some microstructural aspects of both second phases, such as their thermal stability, geometry and size (aspect-ratio) should account for the higher reinforcing capacity of $Mg_6Zn_3Ca_2$ particles with respect to those of I-phase, especially at 200 °C. The melting temperatures of the I- and $Mg_6Zn_3Ca_2$ phases are 450 [4,30,32,76] and 390 °C [32,77-78], respectively. Thus, both second phases are thermally stable over the entire range of test temperatures. Additionally, both phases have a very good interface with the magnesium matrix. It is well known, that I-phase has a quasiperiodic lattice structure that gives it interesting properties such as a low interfacial energy and very good coherence with the magnesium matrix [79], which allows it to be closely linked with the magnesium even during severe deformation processes [80]. Similarly, $Mg_6Zn_3Ca_2$ phase, with a hexagonal structure has a strong matrix/particle interface that enables to preserve good bonding during plastic deformation [81-83]. This fact is evidenced in the micrographs of Fig. 4, where it can be observed that, for all temperature ranges in the deformed regions, cavities hardly formed in matrix/particle interfaces, which is indicative of a good bonding between magnesium and second-phase particles in both alloys.

Precisely the different morphology of I-phase and $Mg_6Zn_3Ca_2$ phases in the as-cast state prior to the extrusion stage accounts for the differences in the size of both phases in the extruded bars. Both-phases are present at the interdendritic regions in the as-cast ingots. However, there are differences in their morphology. In the case of ZW61 alloy, interdendritic regions are thin and discontinuous, mainly constituted by fine lamellar Mg+I-phase eutectics, while a nearly continuous network of $Mg_6Zn_3Ca_2$ locates at the interdendritic regions of as-cast ZW61Ca alloy [32]. During extrusion, the magnesium matrix transfers load into the second phases located at the interdendritic regions until the stress exceeds a critical value at which second phases are broken. Fine lamellae of I-phase break in very fine fragments, while the $Mg_6Zn_3Ca_2$ network leads to a mixture of fine and coarse particles. Fine particles arise from the thinnest part of the $Mg_6Zn_3Ca_2$ network, while coarse particles come from the thicker part of the network.

The size (more specifically, the aspect-ratio) of second-phase particles is essential to understand the effectiveness of load transfer from the magnesium matrix to the second phases. According to a modified shear-lag theory [84], the contribution of the load transfer, when particles are aligned parallel to the applied stress, is done by the following equation:

$$\Delta\sigma_{LT} = \sigma_m \cdot \left(\frac{(L+t).A}{4L}\right).f \quad (6)$$

where σ_m is the stress in the matrix, L the particle length in the stress direction, t the particle diameter, A the particle aspect ratio ($A = L/t$) and f is the volume fraction of second phase particles. In the case of equiaxial particles the stress contribution due to load transfer may be given by:

$$\Delta\sigma_{LT} = \sigma_m \cdot \left(\frac{1}{2}\right).f \quad (7)$$

From Eq.6 it is easy to see the influence of the aspect-ratio as well as the volume fraction of second phases on the load transfer contribution $\Delta\sigma_{LT}$. Besides having a larger volume fraction of second phases, the aspect ratio of $Mg_6Zn_3Ca_2$ is two times higher that of the I-phase. Calculated values for I-phase and $Mg_6Zn_3Ca_2$ phase were $3\sigma_m$ and $7\sigma_m$, respectively, so $Mg_6Zn_3Ca_2$ phase will be more effective as load transfer reinforcement than I-phase.

Based on the calculation of the internal stresses in the course of the compression tests, it is clear that second phases assume an additional stress, which is transferred from the magnesium matrix. Furthermore, the nature, morphology and size of the second phase determine the magnitude of the stress transferred towards the second phase. Such stress is maximized for the $Mg_6Zn_3Ca_2$ phase, disregarding the temperature: up to 300 MPa at room temperature, 260 MPa at 100 °C and 160 MPa at 200 °C. These values are much higher than that found for the I-phase: 170 MPa and 41 MPa at RT and 100 °C, respectively, while it does not bear additional stress at 200 °C. These data clearly demonstrate that magnesium can transfer more effectively stress towards the $Mg_6Zn_3Ca_2$ phase.

Above 200/250 °C, both alloys yield at very low stresses but the ductility is considerably increased, with elongations exceeding 100%. Usually, the maximum elongation is achieved at 300 °C, with elongations of about 300%. The microstructural evolution during the plastic deformation feature resembles rather well with microstructural changes reported during superplastic deformation of Mg–Ni–Y–RE alloys containing high volume fractions of second phases [85-87]. The mechanism controlling the deformation is grain boundary sliding (GBS), which is not prevented for the ZW61Ca alloy for the presence of coarse particles. This indicates the occurrence of sliding not only between neighbour magnesium grains, but also between the magnesium grains in contact with coarse $Mg_6Zn_3Ca_2$ particles. As deformation proceeds, dislocations are generated at both sides of the sliding interfaces. These dislocations cannot be removed from the sliding interface in coarse particles, so concentration of stresses becomes enormous at local points of the interface, which leads to multiple cracking of coarse particles. It is interesting to note that such cracking takes place when the applied stress is very low (10–25 MPa at 300 °C). Then, fine particles are redistributed in the magnesium matrix because GBS involves the rotation of magnesium grains [87].

Growth of magnesium grains in the course of the superplastic regime can cause grain boundary sliding becoming not operative at local regions. There, cavities can be generated, whose coalescence can lead to the premature failure of the material. Since grain coarsening is accelerated at 350 °C, the maximum elongation is exhibited at 300 °C.

5. Conclusions

The influence of calcium addition to the ternary Mg–6Zn–1Y alloy on the mechanical properties at high temperatures has been studied. The following conclusions can be drawn:

- Small addition of calcium to the ternary Mg–6Zn–1Y alloy noticeably improves the mechanical properties in the temperature range (100–300 °C).
- In-situ synchrotron diffraction experiments have shown to be very useful to analyse the load partitioning between the second phases and the magnesium matrix. The aspect-ratio and the nature of second-phase particles, I-phase for ZW61 alloy and $Mg_6Zn_3Ca_2$ for ZW61Ca alloy, determine the effectiveness of load transfer from the magnesium matrix to the second phases. The effect of second-phase volume fraction prevails at low temperatures but the nature of the second phases becomes more important as the temperature increases.
- The stress assumed by $Mg_6Zn_3Ca_2$ particles is much higher than that by the I-phase. Moreover, the strengthening effect of $Mg_6Zn_3Ca_2$ extends up to 200 °C, while I–phase loses its reinforcing effect at 200 °C.
- Above 200 °C the alloys behave superplastically through a complex mechanism which involves cracking of coarse second phase particles. Fine particles favour operation of grain boundary sliding mechanism through the rotation of magnesium grains, which results in an homogeneous distribution of second phases in the magnesium matrix.

Declaration of Competing Interest

None.

Acknowledgements

The authors would like to acknowledge financial support of the Spanish Ministry of Science and Innovation under project number MAT2016-78850-R. We would like to acknowledge the expert support of A. García, A. Tomás and M. Maier for assistance with SEM. The Deutches Elektronen-Synchrotron DESY is acknowledged for the provision of beamtime at the P07 beamline of the PETRA III synchrotron facility in the framework of proposal I-20170054EC.

References

[1] B.L. Mordike, T. Ebert, Mater. Sci. Eng. A 302 (2001) 37–45 http://dx.doi.org/10.1016/S0921-5093(00)01351-4.
[2] A.A. Luo, Int. Mater. Rev. 49 (2004) 13–30 http://dx.doi.org/10.1179/095066004225010497.
[3] M.K. Kulekci, Int. J. Adv. Manuf. Technol. 39 (2008) 851–865 http://dx.doi.org/10.1007/s00170-007-1279-2.
[4] D.H. Bae, M.H. Lee, K.T. Kim, W.T. Kim, D.H. Kim, J. Alloys Compd. 342 (2002) 445–450 http://dx.doi.org/10.1016/S0925-8388(02)00273-6.
[5] A. Singh, M. Nakamura, M. Watanabe, A. Kato, A.P. Tsai, Scr. Mater. 49 (2003) 417–422 http://dx.doi.org/10.1016/S1359-6462(03)00305-1.
[6] A. Singh, M. Watanabe, A. Kato, A.P. Tsai, Mater. Sci. Eng. A 385 (2004) 382–396 http://dx.doi.org/10.1016/j.msea.2004.06.059.
[7] A. Müller, G. Garcés, P. Pérez, P. Adeva, J. Alloys Compd. 443 (2007) 1–5 http://dx.doi.org/10.1016/j.jallcom.2006.10.006.
[8] J.Y. Lee, H.K. Lim, W.T. Kim, D.H. Kim, Mater. Sci. Eng. A 449–451 (2007) 987–990 http://dx.doi.org/10.1016/j.msea.2006.03.141.
[9] G. Garcés, A. Müller, E. Oñorbe, P. Pérez, P. Adeva, J. Mater. Proc. Technol. 206 (2008) 99–105 http://dx.doi.org/10.1016/j.jmatprotec.2007.12.014.
[10] E. Mora, G. Garcés, E. Oñorbe, P. Pérez, P. Adeva, Scr. Mater. 60 (2009) 776–779, doi:10.1016/j.scriptamat.2009.01.012.
[11] S. Zhen-guo, N. Xiao-dong, A.N. Jian, L.I. Guang-yu, Trans. Nonferr. Metal Soc. China 20 (2010) 43–46 http://dx.doi.org/10.1016/S1003-6326(09)60094-7.
[12] K. Hagihara, A. Kinoshita, Y. Sugino, M. Yamasaki, Y. Kawamura, H.Y. Yasuda, Y. Umakoshi, Acta Mater. 58 (2010) 6282–6293 http://dx.doi.org/10.1016/j.actamat.2010.07.050.
[13] C. Bin, L.U. Chen, L.I.N. Dongliang, Z.E.N.G. Xiaoqin, J. Rare Earths 29 (2011) 902–906 http://dx.doi.org/10.1016/S1002-0721(10)60564-9.
[14] A. Singh, Y. Osawa, H. Somekawa, T. Mukai, Scr. Mater. 64 (2011) 661–664 http://dx.doi.org/10.1016/j.scriptamat.2010.12.016.
[15] P. Pérez, J. Medina, G. Garcés, P. Adeva, Intermetallics 31 (2012) 196–201 http://dx.doi.org/10.1016/j.intermet.2012.07.005.
[16] G. Garcés, E. Oñorbe, F. Dobes, P. Pérez, J.M. Antoranz, P. Adeva, Mater. Sci. Eng. A 539 (2012) 48–55 http://dx.doi.org/10.1016/j.msea.2012.01.023.
[17] G. Garcés, D.G. Morris, M.A. Muñoz-Morris, P. Perez, D. Tolnai, C. Mendis, A. Stark, H.K. Lim, S. Kim, N. Schell, P. Adeva, Acta Mater. 94 (2015) 78–86 http://dx.doi.org/10.1016/j.actamat.2015.04.048.
[18] M. Okayasu, S. Takeuchi, M. Matsushita, N. Tada, M. Yamasaki, Y. Kawamura, Mater. Sci. Eng. A 652 (2016) 14–29 http://dx.doi.org/10.1016/j.msea.2015.11.069.
[19] J. Medina, P. Pérez, G. Garcés, P. Adeva, Mater. Charact. 129 (2017) 195–206 http://dx.doi.org/10.1016/j.matchar.2017.04.033.

[20] J. Zhu, X.H. Chen, L. Wang, W.Y. Wang, Z.K. Liu, J.X. Liu, X.D. Hui, J. Alloys Compd. 703 (2017) 508–516 http://dx.doi.org/10.1016/j.jallcom.2017.02.012.
[21] G. Garcés, K. Máthis, J. Medina, K. Horváth, D. Drozdenko, E. Oñorbe, P. Dobroň, P. Pérez, M. Klaus, P. Adeva, Int. J. Plast. 106 (2018) 107–128 https://doi.org/10.1016/j.ijplas.2018.03.004.
[22] J. Medina, P. Pérez, G. Garcés, A. Stark, N. Schell, P. Adeva, Mater. Sci. Eng. A 715 (2018) 92–100 https://doi.org/10.1016/j.msea.2017.12.111.
[23] G. Garcés, K. Máthis, R. Barea, J. Medina, P. Pérez, A. Stark, N. Schell, P. Adeva, Mater. Sci. Eng. A 768 (2019) 138452 https://doi.org/10.1016/j.msea.2019.138452.
[24] G. Garces, A. Orozco-Caballero, J. Quinta da Fonseca, P. Perez, J. Medina, A. Stark, N. Schell, P. Adeva, Mater. Sci. Eng. A 772 (2020) 138716 https://doi.org/10.1016/j.msea.2019.138716.
[25] F.S. Pierce, S.J. Poon, Q. Guo, Science 261 (1993) 737–739 http://dx.doi.org/10.1126/science.261.5122.737.
[26] J.M. Dubois, P. Plaindoux, E. Berlin-Ferre, N. Tamura, D.J. Sordelet, in: Proceedings of the 6th International Conference on Quasicrystals, World Scientific, Singapore, 1997, p. 733.
[27] D.H. Bae, S.H. Kim, D.H. Kim, W.T. Kim, Acta Mater. 50 (2002) 2343–2356 https://doi.org/10.1016/S1359-6454(02)00067-8.
[28] G. Yuan, K. Amiya, H. Kato, A. Inoue, J. Mater. Res. 19 (2004) 1531–1538 https://doi.org/10.1557/JMR.2004.0205.
[29] G. Yuan, H. Kato, K. Amiya, A. Inoue, J. Mater. Res. 20 (2005) 1278 http://dx.doi.org/10.1557/JMR.2005.0156.
[30] D.H. Bae, Y. Kim, I.J. Kim, Mater. Lett. 60 (2006) 2190–2193 http://dx.doi.org/10.1016/j.matlet.2005.12.096.
[31] D.K. Xu, T.T. Zu, M. Yin, Y.B. Xu, E.H. Han, J. Alloys Compd. 582 (2014) 161–166 https://doi.org/10.1016/j.jallcom.2013.08.020.
[32] J. Medina, P. Pérez, G. Garces, D. Tolnai, A. Stark, N. Schell, P. Adeva, Mater. Charact. 118 (2016) 186–198 http://dx.doi.org/10.1016/j.matchar.2016.05.019.
[33] T.V. Larionova, W.-.W. Park, B.-.S. You, Scr. Mater. 45 (2001) 7–12 http://dx.doi.org/10.1016/S1359-6462(01)00982-4.
[34] T. Ebert, K.U. Kainer, 2003, pp. 164–183 http://dx.doi.org/10.1002/3527602046.ch10.
[35] X. Gao, S.M. Zhu, B.C. Muddle, J.F. Nie, Scr. Mater. 53 (2005) 1321–1326 http://dx.doi.org/10.1016/j.scriptamat.2005.08.035.
[36] M. Suzuki, K. Tsuchida, K. Maruyama, Mater. Trans. 49 (5) (2008) 918–923 http://dx.doi.org/10.2320/matertrans.MC200722.
[37] S. Guan, J. Hu, L. Wang, S. Zhu, H. Wang, J. Wang, L. Wen, Z. Ren, S. Chen, E. Meng, J. Gao, S. Hou, B. Wang, B. Che, 2009, pp. 109–152 http://dx.doi.org/10.5772/13187.
[38] L. Geng, B.P. Zhang, A.B. Li, C.C. Dong, Mater. Lett. 63 (2009) 557–559 http://dx.doi.org/10.1016/j.matlet.2008.11.044.
[39] G.T. Bae, J.H. Bae, D.H. Kang, H. Lee, N.J. Kim, Met. Mater. Int. 15 (2009) 1–5 http://dx.doi.org/10.1007/s12540-009-0001-3.
[40] M.-.B. Yang, L. Cheng, F.-.S. Pan, Trans. Nonferr. Metal Soc. China 20 (2010) 769–775 http://dx.doi.org/10.1016/S1003-6326(09)60212-0.
[41] Y. Chen, H. Liu, R. Ye, G. Liu, Mater. Sci. Eng. A 587 (2013) 262–267 http://dx.doi.org/10.1016/j.msea.2013.07.092.
[42] M. Yang, J. Zhang, T. Guo, Mater. Des. 52 (2013) 274–283 http://dx.doi.org/10.1016/j.matdes.2013.05.049.
[43] Q. Wen, K. Deng, J. Shi, B. Zhang, W. Liang, Mater. Sci. Eng. A 609 (2014) 1–6 http://dx.doi.org/10.1016/j.msea.2014.04.093.
[44] B.P. Zhang, L. Geng, L.J. Huang, X.X. Zhang, C.C. Dong, Scr. Mater. 63 (2010) 1024–1027 https://doi.org/10.1016/j.scriptamat.2010.07.038.
[45] B. Zhang, Y. Wang, L. Geng, C. Lu, Mater. Sci. Eng. A 539 (2012) 56–60 http://dx.doi.org/10.1016/j.msea.2012.01.030.
[46] J. Bohlen, J. Wendt, M. Nienaber, K.U. Kainer, L. Stutz, D. Letzig, Mater. Charact. 101 (2015) 144–152 http://dx.doi.org/10.1016/j.matchar.2015.02.002.
[47] F. Li, W.Y. Peh, V. Nagarajan, M.K. Ho, A. Danno, B.W. Chua, M.J. Tan, Mater. Des. 99 (2016) 37–43 http://dx.doi.org/10.1016/j.matdes.2016.03.014.
[48] S. Tekumalla, M. Gupta, Mater. Des. 113 (2017) 84–98 http://dx.doi.org/10.1016/j.matdes.2016.09.103.
[49] Z. Yu, Y. Huang, W. Gan, C.L. Mendis, Z. Zhong, H.G. Brokmeier, N. Hort, J. Meng, Mater. Sci. Eng. A 657 (2016) 259–268 https://doi.org/10.1016/j.msea.2016.01.071.
[50] W. Wu, C.-.P. Chuang, D. Qiao, Y. Ren, K. An, J. Alloys Compd. 683 (2016) 619–633 https://doi.org/10.1016/j.jallcom.2016.05.144.
[51] S. Gavras, T.S. R.H.Buzolin, A. Stark, D. Tolnai, Min. Met Mater Ser. (2017) 675–681 https://doi.org/10.1007/978-3-319-52392-7_93.
[52] S. Gavras, T.S. R.H.Buzolin, A. Stark, D. Tolnai, Materials 11 (2018) 169–175 https://doi.org/10.3390/ma11071103.
[53] H.J. Bong, X. Hu, Y.Ren X.Sun, R.K. Mishra, J. Phys. 1063 (2018) https://doi.org/10.1088/1742-6596/1063/1/012031.
[54] D.S. Gavras, R.H.Buzolin T.Subroto, N. Hort, D. Tolnai, Int. J. Metalcast. 12 (2018) 428–433 https://doi.org/10.1007/s40962-017-0174-3.
[55] E. Oñorbe, G. Garcés, P. Pérez, S. Cabezas, M. Klaus, C. Gencel, E. Frutos, P. Adeva, Scr. Mater. 65 (2011) 719–722 https://doi.org/10.1016/j.scriptamat.2011.07.017.
[56] J. Wang, L. Wang, G. Zhu, B. Zhou, T. Ying, X. Zhang, Q. Huang, Y. Shen, X. Zeng, H. Jiang, Metall. Mater. Trans. A Phys. Metall. Mater. Sci. 49 (2018) 5382–5392 https://doi.org/10.1007/s11661-018-4881-z.
[57] G. Garcés, J. Medina, P. Pérez, K. Máthis, K. Horváth, A. Stark, N. Schell, P. Adeva, Acta Mater. 151 (2018) 271–281 https://doi.org/10.1016/j.actamat.2018.03.060.
[58] S. Kleiner, P.J. Uggowitzer, Mater. Sci. Eng. A 379 (2004) 258–263 https://doi.org/10.1016/j.msea.2004.02.020.
[59] S.R. Agnew, D.W. Brown, C.N. Tome, Acta Mater. 54 (2006) 4841–4852 https://doi.org/10.1016/j.actamat.2006.06.020.
[60] A.P. Tsai, A. Niikura, A. Inoue, T. Masumoto, Y. Nishida, K. Tsuda, M. Tanaka, Phil. Mag. Lett. 70 (1994) 169–175 https://doi.org/10.1080/09500839408240971.
[61] E. Abe, A.P. Tsai, Phys. Rev. Lett. 83 (1999) 753–756 https://doi.org/10.1103/PhysRevLett.83.753.
[62] D.W. Brown, S.R. Agnew, M.A.M. Bourke, T.M. Holden, S.C. Vogel, C.N. Tome, Mater. Sci. Eng. A 399 (2005) 1–12 https://doi.org/10.1016/j.msea.2005.02.016.
[63] M.A. Gharghouri, G.C. Weatherly, J.D. Embury, J. Root, Phil. Mag. 79 (1999) 1671–1695 https://doi.org/10.1080/01418619908210386.
[64] E.A. Brandes, G.B. Brook, Smithells Metals Reference Book, 7th Edition, Butterworth-Heinemann, 1992 Sections 15- 2.
[65] G. Requena, D.C. Yubero, J. Corrochano, J. Repper, G. Garces, Comp. Part A: Appl. Sci. Manuf. 43 (11) (2012) 1981–1988 http://dx.doi.org/10.1016/j.compositesa.2012.07.004.
[66] G. Garcés, E. Oñorbe, P. Pérez, I.A. Denks, P. Adeva, Mater. Sci. Eng. A 523 (2009) 21–26 http://dx.doi.org/10.1016/j.msea.2009.06.026.
[67] G. Garcés, E. Oñorbe, P. Pérez, M. Klaus, C. Genzel, P. Adeva, Mater. Sci. Eng. A 533 (2012) 119–123 https://doi.org/10.1016/j.msea.2011.10.103.
[68] G. Garcés, K. Máthis, P. Pérez, J. Capek, P. Adeva, Mater. Sci. Eng. A 666 (2016) 48–53 https://doi.org/10.1016/j.msea.2016.04.028.
[69] S. Takeuchi, K. Edagawa, Elsevier, 2008, pp. 267–311 https://doi.org/10.1016/S1570-002X(08)80023-7.
[70] J. Du, A. Zhang, Z. Guo, M.Li M.Yang, S. Xiong, Intermetallics 95 (2018) 119–129, doi:10.1016/j.intermet.2018.02.005.
[71] S. Ganeshan, S.L. Shang, H. Zhang, Y. Wang, M. Mantina, Z.K. Liu, Intermetallics 17 (2009) 313–318 https://doi.org/10.1016/j.intermet.2008.11.005.
[72] A.K. Mukherjee, J.E. Bird, J.E. Dorn, Trans. ASM 62 (1969) 155–179.
[73] U.M. Chaudry, T.H. Kim, S.D. Park, Y.S. Kim, K. Hamad, J.-.G. Kim, Mater. Sci. Eng. A 739 (2019) 289–294 https://doi.org/10.1016/j.msea.2018.10.060.
[74] U. M.Chaudry, T.H. Kim, S.D. Park, Y.S. Kim, K. Hamad, J.-.G. Kim, Materials (Basel) 11 (2018) 2201 https://doi.org/10.3390/ma11112201.
[75] T. Mukai, D. Orlov, V. Joshi, K. Solanki, N. Neelameggham (Eds.), The Minerals, Metals & Materials Series. Springer, Cham, 2018 TMS 2018 https://doi.org/10.1007/978-3-319-72332-7_14 .
[76] X. Zeng, Y. Zhang, C. Lu, W. Ding, Y. Wang, Y. Zhu, J Alloys Compd. 395 (2005) 213–219 http://dx.doi.org/10.1016/j.jallcom.2004.10.070.

[77] M. Hradilová, D. Vojtěch, J. Kubásek, J. Čapek, M. Vlach, Mater. Sci. Eng. A 586 (2013) 284–291 http://dx.doi.org/10.1016/j.msea.2013.08.008.
[78] Y.Z. Du, M.Y. Zheng, X.G. Qiao, K. Wu, X.D. Liu, G.J. Wang, X.Y. Lv, Mater. Sci. Eng. A 582 (2013) 134–139 http://dx.doi.org/10.1016/j.msea.2013.06.027.
[79] S. Takeuchi, in: J.M. Dubois, P.A. Thiel, A.P. Tsai, K. Urban (Eds.), Quasicrystals, Proceedings of the Materials Research Society Symposium, 553, Materials Research Society, 1999, p. 283.
[80] D.K. Xu, W.N. Tang, L. Liu, Y.B. Xu, E.H. Han, J. Alloys Compd. 432 (2007) 129–134 https://doi.org/10.1016/j.jallcom.2006.05.123.
[81] G. Levi, S. Avraham, A. Zilberov, M. Bamberger, Acta Mater. 54 (2006) 523–530 https://doi.org/10.1016/j.actamat.2005.09.023.
[82] K. Oh-ishi, R. Watanabe, C.L. Mendis, K. Hono, Mater. Sci. Eng. A 526 (2009) 177–184 https://doi.org/10.1016/j.msea.2009.07.027.
[83] Y.N. Zhang, X.D. Liu, Z. Altounian, M. Medraj, Scr. Mater. 68 (2013) 647–650 https://doi.org/10.1016/j.scriptamat.2012.12.028.
[84] R.M. Aikin, JOM 49 (1997) 35–39 https://doi.org/10.1007/BF02914400.
[85] P. Pérez, S. González, G. Garcés, G. Caruana, P. Adeva, Mater. Sci. Eng. A 485 (1–2) (2008) 194–199 Issue https://doi.org/10.1016/j.msea.2007.07.083.
[86] P. Pérez, M. Eddahbi, S. González, G. Garcés, P. Adeva, Scr. Mater. 64 (2011) 33–36 https://doi.org/10.1016/j.scriptamat.2010.08.059.
[87] S. González, P. Pérez, G. Garcés, P. Adeva, Mater. Sci. Eng. A 673 (2016) 266–276 https://doi.org/10.1016/j.msea.2016.07.077.